

Green's Function Technique for Studying Electron Flow in 2D Mesoscopic Samples

G. Matalidis and P. Bruno^yMax-Planck-Institut für Mikrostrukturphysik, Weinberg 2, D-06120 Halle, Germany^z

(Dated: February 8, 2020)

In a recent series of scanning probe experiments, it became possible to visualize local electron flow in a two-dimensional electron gas. In this paper, a Green's function technique is presented that enables efficient calculation of the quantity measured in such experiments. Efficient means that the computational effort scales like M^3N (M is the width of the tight-binding lattice used, and N is its length), which is a factor MN better than the standard recursive technique for the same problem. Moreover, within our numerical framework it is also possible to calculate (with the same computational effort M^3N) the local density of states, the electron density, and the current distribution in the sample, which are not accessible with the standard recursive method. Furthermore, a new imaging method is proposed where the scanning tip can be used to measure the local chemical potential. The numerical technique is illustrated with some examples.

I. INTRODUCTION

Electronic transport properties in mesoscopic systems have gained a lot of attention in the last two decades (for a review see e.g. Refs. 1,2). A lot of effort already went into the study of global transport quantities (mainly conductance), and a range of interesting phenomena emerged: e.g. quantized conductance in a point contact³, quantum Hall effect⁴, and universal conductance fluctuations⁵ to name a few.

Recently, scanning probe methods have offered the interesting possibility of obtaining local information on electron transport, not accessible with ordinary global measurements. For example, by using the tip of an STM as a localized scatterer of electrons and measuring the conductance change of the sample as a function of tip position, it has been possible to obtain a spatial map of electron flow in a two-dimensional electron gas^{6,7,8}. Such visualizations of current flow are interesting both from an experimental and a theoretical point of view.

The results obtained in these experiments were mainly interpreted with the help of electron or flux density calculations. Here, a numerical technique is developed that allows to calculate in an efficient way the quantity that is actually measured, which is a conductance difference as a function of the tip position. The standard recursive Green's function method used in Ref. 10 to obtain the same result is not very efficient because one has to start over the complete conductance calculation for every position of the tip. The numerical effort in this case scales like M^4N^2 , where M is the width and N is the length of the system ($N \gg 1$), and one therefore is limited to small systems. On the other hand, our method scales like M^3N in the number of operations for the same problem. Moreover, with our method it is straightforward to obtain other relevant information like the local density of states and the electron and current density distributions which can then be compared with the experimental observables. All these quantities can be calculated with a computational effort that scales like M^3N .

It will also be shown that the imaging technique with the tip as a scatterer will not always give the expected

results in the regime of high magnetic fields. To obtain more information about electron flow in this high field range, a new measuring method is proposed where an STM tip is used as a local voltage probe. This method can also be treated within the proposed numerical framework, with a computational effort scaling again as M^3N .

The paper is subdivided as follows. In the next section, the imaging method used in Refs. 6,7 is briefly reviewed and the new voltage probe method is proposed. In section III, we discuss how the considered systems can be described within a tight-binding model. Subsequently, the numerical method is presented in detail in section IV, and it is then applied to some test examples.

II. IMAGING METHODS

A. Tip as a Local Scatterer

The experiments in Refs. 6,7 take place as follows: current is passed via two Ohmic contacts through a two-dimensional electron gas, while simultaneously a scanning probe tip is moved across the sample. The local electrostatic potential that results from a negative voltage on the tip can function as a scattering center for electrons in the device. If the tip is placed over a region where a lot of electrons are flowing, the conductance of the sample will decrease considerably because of enhanced backscattering, whereas in an area of low electron flow, the conductance decrease will be small. As such, by mapping the conductance decrease of the sample to the tip position, one gets a spatial profile of electron flow.

The relevant quantity for this imaging method is thus the position dependent conductance difference:

$$g(x;y) = g_0 - g_t(x;y); \quad (1)$$

where $g_t(x;y)$ is the conductance with the tip positioned on a point $(x;y)$ and g_0 is the conductance without the tip. Conductances can be calculated within the Landauer-Büttiker formalism, which relates conductance to the electron transmission coefficient T between the

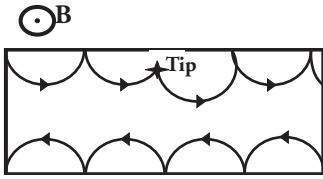


FIG. 1: Schematic view of the cycloidal motion of electrons along the edges of a 2D sample in a strong magnetic field B . Electrons cannot be backscattered by a tip because the paths with opposite propagation direction are well separated.

contacts on opposite sides of the sample:

$$g = \frac{2e^2}{h} T \quad (2)$$

Please note that since g is a two-terminal conductance, it is symmetric with respect to reversal of the direction of an applied magnetic field: $g(+B) = g(-B)$, and therefore the map of electron flow obtained with this scattering method has the same symmetry.

In section IV, a Green's function technique will be presented that allows to efficiently calculate the transmittance T , and thus the conductance, as a function of tip position.

B. Tip as a Voltage Probe

The imaging method in the previous section can give very nice visualizations of the electron flow, as proven by the experimental results of electron transport through a quantum point contact^{6,7}. One of the interesting subjects to study with this imaging method would be the quantum Hall effect, because even after intensive theoretical and experimental effort since its discovery⁴, some of the details of electron transport in this regime remain unclear. Unfortunately, the scattering method will not always yield the expected results in the quantum Hall regime, as will be discussed next.

In a strong magnetic field, the electrons describe cyclotron orbits. If one introduces boundaries to the sample, these orbits will lead to a cycloidal motion of the electrons along the edges of the sample (the so-called edge states), as depicted in Fig. 1. Electrons travelling in opposite directions will be located on opposite sample edges, so the overlap of their wavefunctions will be very small, and this in turn leads to a suppressed backscattering of electrons. The previous imaging method depends precisely on the backscattering by the STM tip, so it can not always give the desired results.

However, if ideal reflectionless contacts are assumed, it is clear from the above picture of edge state transport, that all electrons emanating from the left lead enter the edge states carrying current to the right, and empty in the right contact, while all electrons coming out of the

right contact enter the edge states on the opposite side of the sample and empty in the left contact precisely because there is no backscattering possible. Therefore, edge states carrying current to the right (left) are in equilibrium with the left (right) contact so that one should clearly see different potentials at opposite edges and as such obtain a picture of this edge-state transport by looking at the local chemical potential.

A possible way of measuring the local chemical potential would be to use the STM tip as voltage probe; one measures the voltage on the STM tip when electrons are allowed to tunnel into and out of the tip. Since a voltmeter ideally draws no current, every electron flowing into the STM tip has to leave it on a later time, so that the tip voltage will indeed equilibrate itself to the local chemical potential at the tip position.

Theoretically, one can describe such an experiment again by using the Landauer-Büttiker formalism, but now one has three contacts: the left and right contact through which a fixed current is passed, and the STM tip that measures a voltage. For a multi-lead structure at temperature $T = 0$, one obtains for the currents through the contact leads¹:

$$I_p = \frac{2e^2}{h} \sum_q T_{pq} (V_p - V_q); \quad (3)$$

where p and q label the leads, and T_{pq} is the transmission coefficient from lead q to lead p . Using current conservation ($\sum_p I_p = 0$) and the fact that the current through the STM tip should be zero, one can then express the voltage measured on the STM tip as follows:

$$V_{\text{tip}} - V_L = \frac{T_{\text{tip};L}}{T_{\text{tip};L} + T_{\text{tip};R}} (V_R - V_L); \quad (4)$$

Our numerical method thus should be able to calculate the transmission coefficients $T_{\text{tip};L(R)}$ from the left and right contact to the STM tip, as a function of the position of the tip.

It should be indicated that this imaging mode corresponds to making a three-terminal measurement. This means that the spatial map one obtains will not be invariant under the reversal of the direction of an applied magnetic field, which was the case for the original method in the previous section. The only symmetry relations that hold are: $T_{pq}(+B) = T_{qp}(-B)$. Therefore, it should be clear that the information obtained when the tip is used as a voltage probe is different from that when the tip is used as a local scatterer, and as such both imaging methods will contribute differently to our understanding of electron flow in 2D systems.

C. Charge and Current Density

One can (at least in principal) experimentally observe the total current density in the sample, by measuring

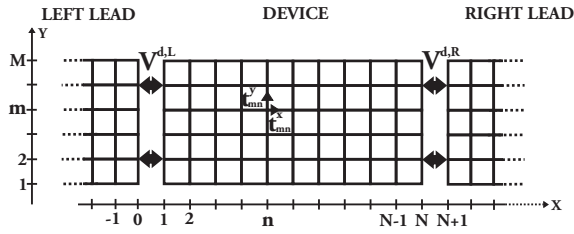


FIG. 2: Tight binding description of the device. The device extends from column $n=1$ to N , and has a total width of M rows. It is connected to semi-infinite leads at the left and right by the hopping matrices $V^{d,L(R)}$.

the magnetic field it induces. Another physically observable quantity is the total charge density, due to the electrostatic field it generates. Both of these quantities can also be calculated within the numerical framework

presented in the next sections. Since we have access to the electron density, it would also be possible to include self-consistently the effect of the applied voltage and the resultant current flow on the transport properties. However, this will not be done in the current paper.

III. SYSTEM MODELING

A. Tight-Binding Model

The system we will consider is a two-dimensional device connected to two semi-infinite leads extending in the x -direction. By discretizing the Schrodinger equation, one obtains the standard nearest neighbor tight-binding model for the system Hamiltonian:

$$H = \sum_{n=1}^N \sum_{m=1}^M \epsilon_{mn} |n;n\rangle \langle n;n| + \sum_{n=1}^N \sum_{m=1}^M t_{mn}^x |n;n+1\rangle \langle n;n| + \sum_{n=1}^N \sum_{m=1}^M t_{mn}^y |n;n\rangle \langle n;n+1| + h.c. : \quad (5)$$

where $(m;n)$ label the sites on the lattice, and ϵ_{mn} are the on-site energies. Note that the sites are not meant to represent atoms as in the usual tight-binding model; rather they may represent a region containing many atoms, but this region should be small with respect to physically relevant quantities such as the Fermi wavelength. The quantities t_{mn}^x and t_{mn}^y in Eq. (5) give the hopping amplitude in the horizontal, respectively vertical direction (see Fig. 2). A square lattice is assumed, so in the absence of a magnetic field one has (magnetic field is treated further down):

$$t_{mn}^x = t_{mn}^y = t = \frac{\hbar^2}{2m a^2}; \quad (6)$$

with a the lattice spacing, and m the effective mass of the electron.

The leads extend from $n=1;::0$ for the left lead, and $n=N+1;::1$ for the right one. The device itself is comprised by the other $M-N$ sites (Fig. 2). The Hamiltonian of the complete system can thus be divided in several parts:

$$H = H^L + H^R + H^d + (V^{d;R} + V^{d;L} + h.c.); \quad (7)$$

with $H^{L(R)}$ describing the semi-infinite leads, H^d the Hamiltonian of the isolated device, and $V^{d;R(L)}$ describing the hopping from the device to the right (left) lead.

B. The Semi-Infinite Leads

The leads are assumed to be ideal, so their potential is translationally invariant along the x -axis. This constrains the on-site energies to be independent of the column index. Furthermore, the energies are also offset by $4t$ in order to shift the bottom of the energy band to 0:

$$\epsilon_{mn} = 4t + \epsilon_m; \quad (8)$$

Only homogeneous fields perpendicular to the 2D device will be considered in the leads, and these can be described by the standard Peierls substitution:

$$t_{mn}^{x(y)} = t e^{ie \int_{\mathbf{r}_m}^{\mathbf{r}_n} \mathbf{A} \cdot d\mathbf{l}}; \quad (9)$$

where $\int_{\mathbf{r}_m}^{\mathbf{r}_n} \mathbf{A} \cdot d\mathbf{l}$ is the integral of the vector potential along the hopping path. Translational invariance along the x -axis can be conserved by using the Landau gauge with vector potential $\mathbf{A} = (By; 0; 0)$. One finds:

$$t_{mn}^x = t e^{2i(m-1)\pi y/a}; \quad t_{mn}^y = t; \quad (10)$$

with $\pi = Ba^2$ the magnetic flux per unit cell, and $\phi_0 = h/e$ the magnetic flux quantum.

Finally, one obtains for the Hamiltonian describing the right lead:

$$H^R = \sum_{n=N+1}^X \sum_{m=1}^X (4t + \Phi_m) j_n ; n ; i m ; n j + (t e^{i 2 \Phi_m}) = \sum_{m=1}^X j_n ; n + 1 ; i m ; n j - t j_n + 1 ; n ; i m ; n j + \text{h.c.} ; \quad (11)$$

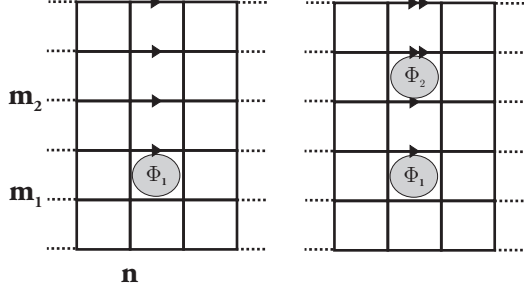


FIG. 3: Including an arbitrary magnetic field in the device can be done by considering flux tubes localized on single lattice cells. For a single flux tube, all hopping parameters above it change their phase by Φ_1 (single arrow on the left drawing). If a second flux tube is included above the first one, hopping parameters located above both cells will change their phase by $\Phi_1 + \Phi_2$ (double arrows on the right).

and an equivalent expression for the left lead, with the summation over n going from -1 to 0 .

Until now, in most tight-binding based numerical calculations, one has only considered homogeneous fields. Including the influence of such a field with the Peierls substitution in the Landau gauge, like discussed above, is very convenient, but in the central device we would like to be able to include inhomogeneous fields. In the next section, a method for describing these in a tight-binding description will be presented.

C. Inhomogeneous Magnetic Fields in the Device

The Peierls substitution method gives a very convenient way of dealing with magnetic fields in a tight-binding model. However, it is not always clear what vector potential A to choose for a particular magnetic field distribution. It is for instance not obvious what a good choice for A looks like when one has a completely random magnetic field in the device. Nevertheless, we have found a convenient way of arranging things for any possible field distribution. This is explained in Fig. 3. Suppose that one has a perpendicular magnetic field with strength B , that is localized on a single lattice cell and zero outside, as in Fig. 3. The influence of this local field can be described by changing all the hopping parameters $t_{m,n}^x$ above the flux tube as follows:

$$t_{m,n}^x \rightarrow t e^{i 2 \Phi_m} ; \quad (12)$$

where Φ_1 is the total flux enclosed by the unit cell that encompasses the local field, $\Phi_1 = B_1 a^2$. This is indicated

by the single arrows in Fig. 3. For every closed path that encloses the flux tube, the total phase of an electron travelling along the path will then change by $2 e \hbar^{-1} \Phi_1$, so this gives a correct description of the field. A second localized flux tube in the same column n as the previous one will contribute another phase change Φ_2 , but again only to the hopping parameters above the second flux tube. The total change of the hopping parameters is then the sum of both contributions, so that one finds (see Fig. 3):

$$t_{m,n}^x \rightarrow \begin{cases} t & ; m < m_1 < m_2 \\ t e^{i 2 \Phi_m} & ; m_1 < m < m_2 \\ t e^{i 2 \Phi_m} & ; m_1 < m_2 < m \end{cases} \quad (13)$$

This line of reasoning can be easily generalized to a situation where every unit cell encompasses a single flux tube. One just changes the hopping parameters as:

$$t_{m,n}^x \rightarrow t e^{i 2 \Phi_m} ; \quad (14)$$

where Φ_m is the flux through the lattice cell above the link connecting site $(m^0; n)$ with site $(m^0; n+1)$. As such, one can describe an arbitrary magnetic field in the device by choosing the appropriate fluxes through the different lattice cells. It is easy to see that the method above will yield the same expression as the Landau gauge in Eq. (10), when we consider a homogeneous field where all lattice cells comprise the same flux $\Phi_m = \Phi = B a^2$.

IV. NUMERICAL METHOD

A. Introduction

In sections IIA and IIB, it was shown that the basic quantities that need to be calculated in order to describe the scanning probe experiments are transmission coefficients from one lead to another. In the next sections, it will be shown that these transmission coefficients, and as a matter of fact all other quantities we wish to calculate (density of states, current density distribution,...) can be expressed in terms of the Green's function matrices G_{n1}^0 , G_{nn}^0 , G_{Nn}^0 and G_{Nn}^0 (for all possible values of n), where the $M \times M$ matrices G_{10}^0 are defined as:

$$i G_{10}^0 j_n^0 i = i G_{10}^0 j_n^0 i ; \quad (15)$$

with

$$G^0 = \frac{1}{E + i \Gamma} \frac{1}{H^d L R} ; \quad (16)$$

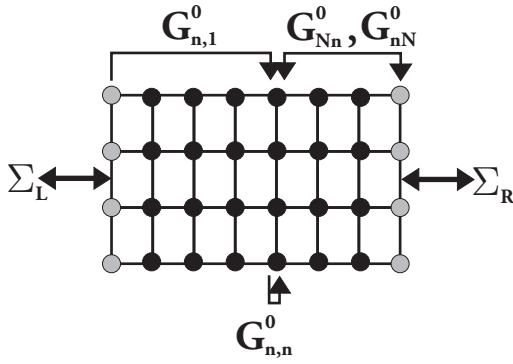


FIG. 4: View on the Green's functions necessary to calculate the relevant physical quantities in our problem. The first and last column of the tight binding lattice are colored grey to indicate that they are influenced by the self-energies Σ_L and Σ_R of the leads.

the Green's function of the device without the influence of the tip (Σ_L and Σ_R are self-energies of the left respectively right lead). The Green's functions G_{1l}^0 are thus submatrices of G^0 connecting points from column l^0 to those of column n^1 (see also Fig. 4).

In the next sections, it will first be shown that indeed all physically relevant quantities can be expressed in terms of the $G_{n1}^0, G_{nn}^0, G_{nN}^0, G_{Nn}^0$, and the self-energies of the leads. The discussion on how to calculate these Green's functions will be delayed to section IV F, while a method for obtaining the self-energies is given in section IV G.

B. Local Scatterer Method

For this imaging method, the tip is used to create an electrostatic potential which scatters electrons. In our calculations, this potential is modelled by a delta function, so the influence of the tip positioned on lattice site $(m;n)$ is to add a repulsive contribution $V^{\text{tip}} = w \delta_{m;n} \delta_{n;n}$ ($w > 0$) to the on-site energies in the Hamiltonian (5). Like explained in section IIA, one has to calculate the conductance difference (see Eqs. (1) and (2)):

$$g(m;n) = \frac{2e^2}{h} [\Gamma^0 - T(m;n)]; \quad (17)$$

for every position $(m;n)$ of the sample in order to obtain the spatial map of electron flow in the sample. One thus needs to calculate the transmittance $T(m;n)$ between the left and right lead for every position of the tip. This transmission coefficient can be calculated by¹:

$$T(m;n) = \text{Tr}[\Sigma_R G_{N1} G_{N1}^Y \Sigma_L]; \quad (18)$$

with $\Sigma_{L(R)}$ related to the retarded self-energies $\Sigma_{L(R)}$ of the left (right) lead (see section IV G) as:

$$\Sigma_{L(R)} = i(\Sigma_{L(R)} - \text{Im} G_{L(R)}^0); \quad (19)$$

and G_{N1} is the Green's function between columns 1 and N . The matrix G_{N1} includes the effect of the STM tip, and is therefore different from G_{N1}^0 , mentioned in the introduction. The transmittance T^0 without the tip can be calculated by replacing G_{N1} by G_{N1}^0 in Eq. (18), but the question is how to find G_{N1} in an efficient way?

In Ref. 10, one uses the standard recursive Green's function method for this: first, the system is divided into its separate columns (by making the hopping matrices between them zero), and subsequently they are attached one by one making use of Dyson's equation (see also Fig. 8 and the discussion in section IV F). This attachment procedure has to be started over and over again for every single position of the tip. Since $N-1$ inversions of an $M \times M$ matrix are needed to obtain G_{N1} for a single tip position, and one has $M \times N$ possible tip locations, the total number of inversions needed to calculate G_{N1} for all positions scales as $M \times N^2$ (in the limit of large N). The computational effort to invert an $M \times M$ matrix scales as M^3 , so the total effort to obtain G_{N1} for all tip locations scales as $M^4 N^2$ with the standard recursive technique.

However, supposed that we have access to the Green's functions G_{n1}^0, G_{Nn}^0 and G_{nn}^0 (see section IV F), we are able to do things more efficient, by including the effect of the tip with Dyson's equation:

$$G = G^0 + G^0 V G; \quad (20)$$

which relates the Green's function G^0 of a Hamiltonian H_0 to the Green's function G of the Hamiltonian $H_0 + V$. In the present case, we will take V as the perturbation introduced by the tip, $V = V^{\text{tip}}$. Projecting Dyson's equation (20) between the columns 1 and N , one obtains (it is assumed that the tip is located at lattice site $(m;n)$):

$$G_{N1} = G_{N1}^0 + G_{Nn}^0 V_{nn}^{\text{tip}} G_{n1}; \quad (21a)$$

$$G_{n1} = G_{n1}^0 + G_{nn}^0 V_{nn}^{\text{tip}} G_{n1}; \quad (21b)$$

with:

$$V_{nn}^{\text{tip}} = w \delta_{m;n} \delta_{n;n}; \quad (22)$$

From Eq. (21b), one obtains:

$$G_{n1} = (1 - G_{nn}^0 V_{nn}^{\text{tip}})^{-1} G_{n1}^0; \quad (23)$$

Putting this into Eq. (21a), the expression for G_{N1} finally becomes:

$$G_{N1} = G_{N1}^0 + G_{Nn}^0 V_{nn}^{\text{tip}} (1 - G_{nn}^0 V_{nn}^{\text{tip}})^{-1} G_{n1}^0 \quad (24)$$

Since V_{nn}^{tip} has only one non-zero element (Eq. (22)), the inversion $(1 - G_{nn}^0 V_{nn}^{\text{tip}})^{-1}$ will boil down to the inversion of a scalar. This means that no extra matrix inversions are needed to find G_{N1} for an arbitrary lattice position of the tip, once we have the G_{Nn}^0 , G_{nn}^0 and G_{n1}^0 for all n ! In section IV F, we will show a way of calculating these functions with a number of matrix inversions that scales linear with N , so that the total computational effort for calculating them scales as $M^3 N$.

At first sight, it might seem that this efficiency is decreased a little bit for the complete calculation because one has to evaluate the trace in Eq. (18) for every tip position, which involves products of $M \times M$ matrices. The computational effort for doing such a product scales like M^3 , and since there are $M N$ lattice sites, the total effort would scale as $M^4 N$. However, there is a better way of arranging things. We write (see Eq. (24)):

$$G_{N1} = G_{N1}^0 + A; \quad (25)$$

with the $M \times M$ matrix:

$$A = G_{Nn}^0 V_{nn}^{\text{tip}} (1 - G_{nn}^0 V_{nn}^{\text{tip}})^{-1} G_{n1}^0 \quad (26)$$

It is important now to make it clear that since V_{nn}^{tip} has only one non-zero element, namely on position $(m;n)$ (Eq. (22)), one can write A as a product of a column matrix and a row matrix:

$$A = [G_{Nn}^0]_{(:,m)} [G_{n1}^0]_{(m,:)}; \quad (27)$$

where we introduced the subscript $(:,m)$ (resp. $(m,:)$) to denote the m^{th} column (row) of a matrix. The scalar is given by:

$$= \frac{w}{1 - w \text{Im} \mathcal{E}_{nn}^0} \quad (28)$$

By substituting Eq. (25) into Eq. (18), one obtains:

$$T(m;n) = T^0 + 2\text{ReTr}[{}_R A {}_L (G_{N1}^0)^Y] + \text{Tr}[{}_R A {}_L A^Y]; \quad (29)$$

So in order to evaluate $T(m;n) - T^0$, which is proportional to the conductance difference $g(m;n)$ we wish to obtain, we need to evaluate only the last two terms in Eq. (29). The last term only involves products of an $M \times M$ matrix with row or column matrices because of the special form of A . The computational effort for this term scales thus as M^2 , which corresponds to a total effort of $M^3 N$ for all tip locations. Now, since ${}_L (G_{N1}^0)^Y$ is independent of the tip position, it has to be calculated only once (with an effort M^3). When this matrix is known, the trace in the second term also contains only products of an $M \times M$ matrix with a row or column matrix, so the computational effort then scales like M^2 , and

as a result the total effort for all tip positions scales like $M^3 N$ in the limit of large N .

From the previous discussion, it becomes clear that the effort for calculating the electron flow map scales like $M^3 N$ in the number of operations. As such, our method is more efficient than the standard recursive technique, which scales like $M^4 N^2$ for the same problem.

C. Voltage Probe Method

In this case, the STM tip will be modelled by a one-dimensional semi-infinite lead, attached to the central device at position $(m;n)$ (the lead can be thought to extend in a direction perpendicular to the 2D sample). At infinity, the lead is attached to an imaginary reservoir. One imposes the constraint that there is no net current through the lead, so for every electron entering the lead, an electron has to pass from the lead back into the device. As such, the chemical potential of the reservoir feeding the 1D lead will equilibrate itself to the local chemical potential at the tip position $(m;n)$ and the extra reservoir functions as a local voltmeter.

We have shown that the voltage on the tip can be written as a function of the transmission coefficients $T_{\text{tip};L}$ and $T_{\text{tip};R}$ between the STM tip and the left and right leads (Eq. (4)). These transmissions, with the tip positioned over site $(m;n)$, can be expressed as:

$$T_{\text{tip};L} = \text{Tr}[{}_{\text{tip}} G_{n1} {}_L G_{n1}^Y]; \quad (30a)$$

$$T_{\text{tip};R} = \text{Tr}[{}_{\text{tip}} G_{nN} {}_R G_{nN}^Y]; \quad (30b)$$

where ${}_{\text{tip}} = i(\frac{y}{x})$. Since the lead modelling the tip is one-dimensional, one does not have to take care of magnetic field effects in this lead, and the self-energy Σ_{tip} of the tip is known analytically¹:

$$\Sigma_{\text{tip}} = t e^{i(A \cos(1 - E = (2t)))}; \quad (31)$$

So we only need to obtain the Green's functions G_{n1} and G_{nN} , which include the tip, in order to obtain the necessary transmission coefficients. The standard recursive Green's function technique only gives access to G_{N1} , so it cannot be used here.

But once again, we can use Dyson's equation (20) to relate the Green's functions G_{n1} and G_{nN} in Eqs. (30) to Green's functions of the device without the tip (calculated in section IV F). Effectively, the influence of the tip will be to add the self-energy Σ_{tip} to the on-site energy ϵ_{mn} in the Hamiltonian of the device. It can thus be described by a "perturbing" imaginary potential

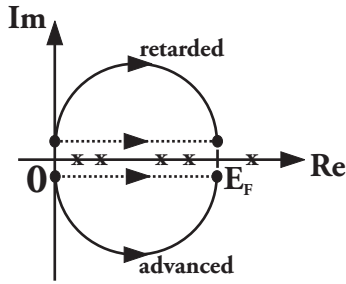


FIG. 5: Integration of the Green's functions in the complex plane. Instead of the ordinary path close to the real axis (dotted line), one can choose a semicircle in the upper (lower) half of the complex plane for a retarded (advanced) function (solid line) because the poles are on the real axis.

$V^{\text{tip}} = t_{\text{tip}} j_n n_{\text{ilm}} n_j$. We end with Dyson's equation:

$$G_{n1} = (1 - G_{nn}^0 V_{nn}^{\text{tip}})^{-1} G_{n1}^0; \quad (32a)$$

$$G_{nN} = (1 - G_{nn}^0 V_{nn}^{\text{tip}})^{-1} G_{nN}^0; \quad (32b)$$

Again, the inversion $(1 - G_{nn}^0 V_{nn}^{\text{tip}})^{-1}$ will reduce to the inversion of a scalar, because V_{nn}^{tip} has only one non-zero element. In section IV F, a method is given for calculating G_{n1}^0 , G_{nn}^0 , G_{nN}^0 and G_{Nn}^0 in an efficient way (computational effort scales as $M^3 N$), so the calculation of the transmissions in Eqs. (30) is completed. In this case, calculation of the traces in Eqs. (30) is not computationally expensive since t_{tip} has only one non-zero element. Therefore the total effort also scales like $M^3 N$.

D. LDOS - Electron Density

In order to compare the visualizations of electron flow obtained by the two imaging methods above with the theory of electron transport, it can be useful to calculate the local density of states (LDOS) and the electron density distribution in the sample, of course without any STM tip over the sample. Expressions for these quantities can be given within our numerical framework in terms of a subset of Green's functions calculated in section IV F. For the LDOS, the standard expression is¹:

$$\rho(E + i; m; n) = \frac{1}{\pi} \text{Im} \text{Im} \int_0^{E_F} \mathcal{G}_{nn}^0(E + i) j_n i; \quad (33)$$

where the energy dependence of the retarded Green's function has been written out explicitly ($\neq 0^+$).

Having calculated the linear density of states, it is also easy to obtain the electron density in the sample by integrating over energy. At temperature $T = 0$, one has:

$$\begin{aligned} \langle m; n \rangle &= \int_0^{E_F} dE \langle m; n; E \rangle \\ &= \frac{1}{\pi} \text{Im} \int_0^{E_F} dE \text{Im} \int_0^{E_F} \mathcal{G}_{nn}^0(E + i) j_n i \end{aligned}$$

From a numerical point of view however, the problem is not as straightforward because a lot of integration points will be needed to reach convergence, e.g. in the quantum Hall regime, where the LDOS has narrow peaks corresponding to the different Landau levels. But, since the Green's function has its poles on the real axis, one can shift the integration path up into the complex plane, allowing to take on finite values. Doing this, one in fact artificially broadens the structures in the linear density of states, leading to faster convergence of the integral. As such, the integration in the complex plane allows for a very efficient method of calculating the electron density. In our calculations, we will use a semicircle as the integration contour, as depicted in Fig 5.

E. Current Density Distribution

1. Equilibrium Current

When no bias is applied, there will be no net current through the leads. However, this does not necessarily mean that the current density distribution will be zero; when a magnetic field is present, persistent currents are flowing through the device. In a recent paper by Crestlet al.¹¹, an expression for the equilibrium current is derived from the Keldysh formalism. Adapted to our notation, the expression for the particle current at temperature $T = 0$ flowing from one node to a neighboring node reads (remember that m labels the rows of the lattice, n the columns):

$$I_{(m;n) \rightarrow (m;n)}^{\text{eq}} = \frac{2e}{\pi} \int_0^{E_F} \frac{dE}{2} 2 \text{Re} \text{Im} j G_{nn}^0 \left(\frac{\text{left}}{n} \right) \left(\frac{\text{left}}{n} \right) G_{nn}^0 j_n i; \quad (35a)$$

$$I_{(m;n) \rightarrow (m+1;n)}^{\text{eq}} = \frac{2e}{\pi} \int_0^{E_F} \frac{dE}{2} 2 \text{Re} \text{Im} + 1 j t_{m;n}^y (G_{nn}^0 - G_{nn}^{0y}) j_n i; \quad (35b)$$

Here, E_F is the Fermi energy of the device (which in equilibrium is equal to the chemical potential in the leads),

and e is the negative electronic charge. We have also

introduced:

$$j_n^{\text{left}} = V_{n,m-1} G_{n-1,m-1}^{0;L} V_{n-1,m}; \quad (36)$$

where the $G_{nn}^{0;L}$ will be defined in section IV F, and are calculated with the Eqs. (43) given there (see also Fig. 8).

It is clear, by taking the trace over the row indices m , that the total current flowing through every single column n is equal to zero, so as expected there will be no net current through the leads. Also, when no magnetic field is present, all Green's functions in Eq. (35) are symmetric so that the equilibrium current density in this case vanishes like it should.

In calculating the equilibrium current, one has to integrate over energy. Calculation of the integrals along the real axis again proves to be very time consuming because of slow convergence, but as we have shown above, this problem can be solved by taking an integration contour in the complex plane. For the longitudinal current $I_{(m,m-1)!(m,m)}^{\text{eq}}$, one can take the same semicircle as before, in the upper half of the complex plane. However, since the transversal current $I_{(m,m)!(m+1,m)}^{\text{eq}}$ contains an advanced Green's function ($G_{nn}^{0;Y}$), the integration path for the part containing this function has to be chosen in the lower half of the complex plane, as shown in Fig. 5.

2. Non-equilibrium Current

In the non-equilibrium situation, we apply a bias voltage so that the chemical potential of one of the leads is higher than that of the other lead. In the present discussion, we will assume that $\mu_L > \mu_R$. In the central device however, the Fermi level is not known a priori, and it should be calculated self-consistently. Nevertheless, in most calculations (ours also), the redistribution of charges in the sample as a result of the current flowing is not taken into account, and one then puts the Fermi energy in the device at a more or less arbitrary level between μ_L and μ_R . In Ref. 11, the total current density in the non-equilibrium situation is divided in what is called an "equilibrium" and a "non-equilibrium" part: $j_{\text{tot}} = j_{\text{eq}} + j_{\text{neq}}$. The equilibrium part is defined as the current arising from states below the Fermi energy in the device, where it is assumed that they are all occupied with electrons. The expression for this equilibrium part is thus equal to Eq. (35), but now E_F has been put somewhere between μ_L and μ_R . On the other hand, the non-equilibrium part is defined as the current resulting from the states with energies between μ_L and μ_R (which are not necessarily all filled with electrons).

Since the position of the Fermi level in the present case (without a self-consistent calculation) is completely arbitrary, this subdivision in an equilibrium and non-equilibrium part is not a physically relevant one, and it can lead to some confusion as to how the non-equilibrium current density distribution looks like. To state that the non-equilibrium density distribution is equal to the one

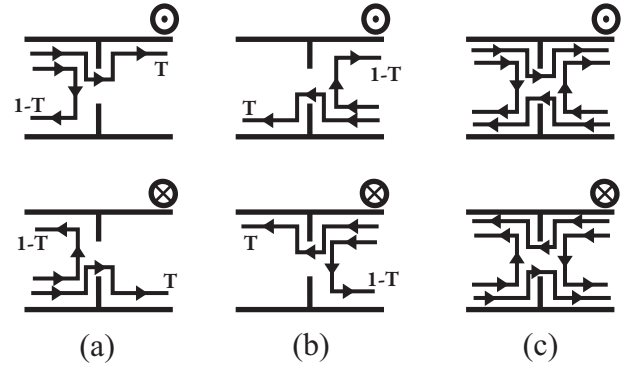


FIG. 6: Scattering states emerging from the left (a) and right (b) lead, for opposite directions of the magnetic field. The equilibrium current density (c) will look like the sum of (a) and (b).

resulting from the non-equilibrium part only is therefore not a relevant picture, because it is dependent on the choice of the Fermi level in the device. This will be made clearer with the help of Fig. 6.

Take as an example a quantum wire with a constriction in the middle, and let's have a look at the scattering states in this system. When a large magnetic field is present, electrons will move along the edges of the system. An electron with a certain energy, emerging from the left lead, has a probability T of reaching the right lead, and a probability $1 - T$ of being reflected. Scattering states emerging from the left are schematically drawn in Fig. 6a. Scattering states for electrons emerging from the right lead are shown in Fig. 6b.

The equilibrium part of the current j_{eq} results from the states below E_F , assumed to be all occupied. So scattering states emerging from the left and the right lead are equally occupied, and one would see a distribution of current for the equilibrium part as shown in Fig. 6c, namely a sum of currents like in Figs. 6a and b.

Turning our attention to the non-equilibrium part j_{neq} , suppose that we have put the Fermi energy in the device E_F equal to μ_R , like in Fig. 7a. The non-equilibrium part of the current distribution then results from the electrons which occupy states between μ_L and μ_R , all emerging from the left lead, so the density distribution for this part will look like in Fig. 7a. Had we put the Fermi energy equal to μ_L as in Fig. 7b, then there would be too much occupied states in the right lead taken into account for the equilibrium part of the current, so the non-equilibrium part should even things out and we should subtract the contribution coming from electrons in scattering states emerging in the right lead with energies between μ_L and μ_R . The current density distribution for the non-equilibrium part then looks like in Fig. 7b; it is the same as that of Fig. 6b, but with the sign reversed because we have to subtract this contribution. Yet another picture emerges when one puts the Fermi energy in the middle between μ_L and μ_R (as in Fig. 7c). In this case, we have taken a too large contribution of currents emerg-

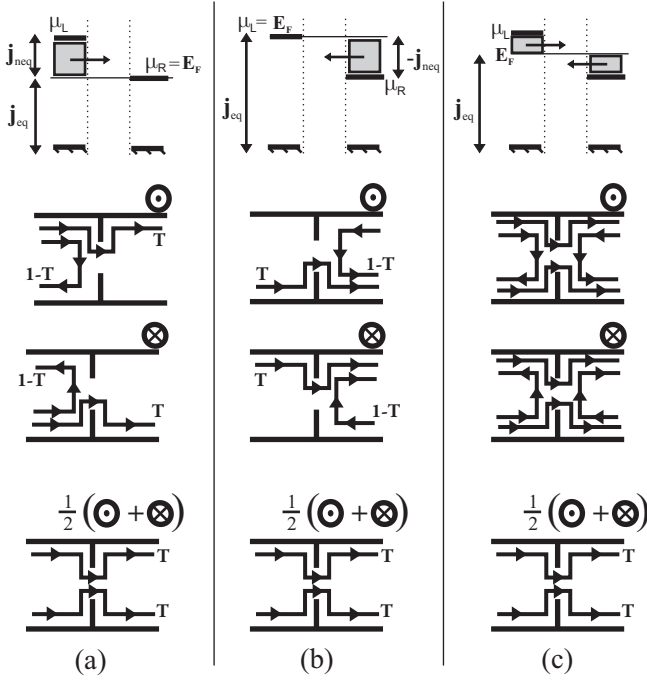


FIG. 7: The "non-equilibrium" part of the current density distribution j_{neq} is dependent upon the choice of E_F in the device. From left to right are shown the distributions that result for $E_F = E_L$ (a), $E_F = E_R$ (b), $E_F = \frac{E_L + E_R}{2}$ (c), and for opposite directions of the magnetic field. Symmetrizing the distributions with respect to the magnetic field direction gives a unique picture whatever the choice of the Fermi level (lowest three pictures).

ing from the right lead, and a too small contribution of currents emerging from the left lead in the equilibrium part, so by evening things out in the non-equilibrium part the current density distribution for this part now looks like Fig. 7c.

It is clear that, depending on where the Fermi level is put in the device, the distribution resulting from the

non-equilibrium part j_{neq} looks completely different. In one picture, it seems that electrons are flowing on the lower side of the sample, in the other pictures they flow on the upper edge or even on both edges. Splitting the current density distribution in an equilibrium and a non-equilibrium part when a bias is applied is not only confusing, but also not physically relevant. Only the sum of both contributions can be attributed a clear physical meaning.

So in order to calculate the current density distribution, it seems that we have to calculate both the equilibrium part and the non-equilibrium part for some value of the Fermi level in the device, and to sum both contributions, because only this sum has a clear physical meaning. The annoying thing about calculating the equilibrium part is that one has to do a time consuming energy integration (which is not necessary for the non-equilibrium part in linear response, as shown below).

However, it should be noted that the equilibrium current is anti-symmetric in the magnetic field, so if one was to calculate the part of the total current density j_{tot} that is symmetric in the field, we only have to symmetrize the non-equilibrium part:

$$j_{\text{tot}} = j_{\text{tot}}(+B) + j_{\text{tot}}(-B) = 2(j_{\text{neq}}(+B) + j_{\text{neq}}(-B)) \quad (37)$$

Moreover, doing this symmetrization gives us a picture for the current density distribution which is unique, whatever choice we make for the value of E_F in the device (see Fig. 7). Furthermore, it can be seen from the figure that the symmetrized part of the current density distribution gives us only that part of the current that is really flowing from one lead into the other. It describes a real "transport" current. So the symmetrized total current density distribution $j_{\text{tot}} = 2(j_{\text{neq}}(+B) + j_{\text{neq}}(-B))$ is a quantity that has a clear physical meaning, and is easy to calculate because no energy integration is necessary in the linear response regime. It is given by (see also Ref. 11):

$$I_{(m,n)! (m,n)}^{\text{neq, sym}} = \frac{2e}{\hbar} \frac{dE}{2} (f_L(E) - f_R(E)) f_A(E) j_B + A(E) j_B g \quad \frac{2e^2 V}{2\hbar} f_A(E) j_B + A(E) j_B g; \quad \text{with} \quad (38a)$$

$$A(E) = 2 \text{Im} \sum_n j G_{nn}^0 \text{right} G_{nn}^{0y} (\text{left})^y j_n i$$

$$I_{(m,n)! (m+1,n)}^{\text{neq, sym}} = \frac{2e}{\hbar} \frac{dE}{2} (f_L(E) - f_R(E)) f_C(E) j_B + C(E) j_B g \quad \frac{2e^2 V}{2\hbar} f_C(E) j_B + C(E) j_B g; \quad \text{with} \quad (38b)$$

$$C(E) = 2 \text{Im} \sum_n j t_{m,n}^y G_{nn}^0 \text{right} G_{nn}^{0y} j_n i$$

where $V = V_L - V_R$ is the potential difference between the leads, f_L and f_R are the Fermi distributions in the

left and right lead respectively, and:

$$G_n^{\text{left}} = V_{n,n-1} G_{n-1,n-1}^{0;L} V_{n-1,n}; \quad (39a)$$

$$G_n^{\text{right}} = V_{n,n+1} G_{n+1,n+1}^{0;R} V_{n+1,n}; \quad (39b)$$

$$G_n^{\text{right}} = i [G_n^{\text{right}} - (G_n^{\text{right}})^y]; \quad (39c)$$

In these expressions, the matrix $V_{n+1,m}$ describes the hopping from slice n to $n+1$:

$$V_{n+1,m} = \begin{pmatrix} 0 & t_{n,1}^x & 0 & & & 1 & 0 \\ 0 & 0 & t_{n,2}^x & 0 & & 0 & 0 \\ \vdots & \ddots & \ddots & \ddots & \ddots & \vdots & \vdots \\ 0 & & & & & 0 & t_{n,M}^x \end{pmatrix}; \quad (44)$$

and $V_{n,m+1} = V_{n+1,m}^y$. Please note that since not all columns are attached to each other in $G_{n1}^{0;L}$ and $G_{nn}^{0;L}$ (only those to the left of column n), these Green's functions are not equal to the Green's functions G_{n1}^0 and G_{nn}^0 we are trying to obtain (an exception of course is $G_{N1}^{0;L}$ which in fact is equal to G_{N1}^0). The superscript L is

added to make this distinction clear.

From Eq. (43) it can be seen that attaching a single isolated column n costs one inversion of an $M \times M$ matrix, so starting from $n=1$ (by definition $G_{1,1}^{0;L} = G_{1,1}^{isol}$) a total of $N-1$ matrix inversions are necessary to calculate the $G_{n1}^{0;L}$ and $G_{nn}^{0;L}$ for all n , starting from the G_{ii}^{isol} .

For the third step, we start over from the isolated Green's functions already calculated in step 1, and glue them together like we did in the previous step on the basis of a Dyson's equation, but now beginning from the right, like depicted in Fig. 9. The Green's functions we calculate with every step are $G_{Nn}^{0;R}$, $G_{nn}^{0;R}$ and $G_{nn}^{0;R}$, which are given in terms of the $G_{N,m+1}^{0;R}$, $G_{n+1,m+1}^{0;R}$ and $G_{n+1,N}^{0;R}$ as:

$$G_{nn}^{0;R} = (1 - G_{nn}^{isol} V_{n,m+1} G_{n+1,m+1}^{0;R} V_{n+1,m})^{-1} G_{nn}^{isol}; \quad (45a)$$

$$G_{Nn}^{0;R} = G_{N,m+1}^{0;R} V_{n+1,m} G_{n,m}^{0;R}; \quad (45b)$$

$$G_{nN}^{0;R} = G_{nn}^{0;R} V_{n,m+1} G_{n+1,N}^{0;R}; \quad (45c)$$

Starting from $G_{NN}^{0;R} = G_{NN}^{isol}$, one can obtain $G_{Nn}^{0;R}$, $G_{nn}^{0;R}$ and $G_{nn}^{0;R}$ for all $n = N-1; N-2; \dots; 1$. Again, a single matrix inversion is needed for the attachment of a single column n , so a total of $N-1$ inversions for the completion of the third step.

The final step is to get the G_{Nn}^0 , G_{nN}^0 , G_{nn}^0 and G_{n1}^0 we are looking for by attaching the previously calculated

Green's functions in pairs, like illustrated in Fig. 9. One takes a section of connected columns 1 to n (with known Green's functions $G_{n1}^{0;L}$ and $G_{nn}^{0;L}$), and attaches it to the section of connected columns $n+1$ to N (with Green's functions $G_{N,m+1}^{0;R}$ and $G_{n+1,m+1}^{0;R}$). The mathematical expressions are:

$$G_{n1}^0 = (1 - G_{nn}^{0;L} V_{n,m+1} G_{n+1,m+1}^{0;R} V_{n+1,m})^{-1} G_{n1}^{0;L}; \quad (46a)$$

$$G_{nn}^0 = (1 - G_{nn}^{0;L} V_{n,m+1} G_{n+1,m+1}^{0;R} V_{n+1,m})^{-1} G_{nn}^{0;L}; \quad (46b)$$

$$G_{Nn}^0 = G_{N,m+1}^{0;R} V_{n+1,m} G_{n,m}^{0;R}; \quad (46c)$$

$$G_{nN}^0 = G_{nn}^{0;R} V_{n,m+1} G_{n+1,N}^{0;R}; \quad (46d)$$

for $n = 1; \dots; N$. Please note that a single inversion is necessary for each pairwise addition, which gives a total of $N-1$ inversions for the final step.

From the previous discussion, it becomes clear that we need $N + 3(N-1)$ inversions for calculating G_{Nn}^0 , G_{nN}^0 , G_{nn}^0 and G_{n1}^0 for all n . So our method scales indeed linear with N in the number of inversions.

G. Self-Energies for the Leads

The Hamiltonian of the system, Eq. (7) comprises infinite leads. The Hamiltonian matrix will therefore be infinite dimensional. The standard way to resolve this problem is to describe the effect of the leads in terms of self-energies. The self-energy of the right lead is given by¹:

$$\Sigma^R = V^{d;R} G_{surf} (V^{d;R})^y; \quad (47)$$

with $V^{d;R}$ describing the hopping matrix from the lead to the device (Eq. (7)), and G_{surf} the surface Green's

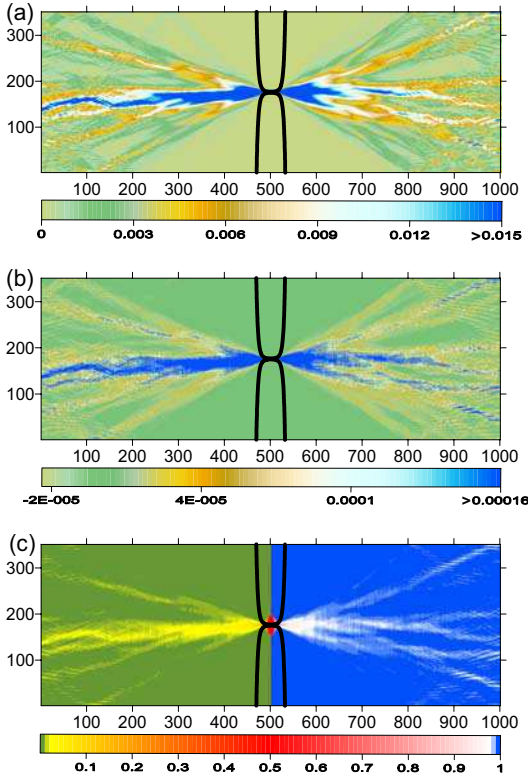


FIG. 10: Maps of electron flow through a quantum point contact. Lengths on the axes are given in units of the lattice parameter a . Current density distribution (a) in units of $2e^2V = (\hbar a)$, STM conductance map (b) (conductance is measured in units of $2e^2 = \hbar$) and STM voltage probe map (c). The voltage on the left lead $V_L = 0$, and voltage is measured in units of V_R . The Fermi energy contour is depicted in black. There is a clear correspondence between the different images.

the repulsive potential from a single impurity is taken to vary with distance r as $1/r^3$, which is characteristic for the screened potential in a 2DEG from a point charge¹⁵. The concentration of impurities is fixed at 1% of the total number of lattice sites. The impurity lattice is located at a distance $9a$ above the 2DEG. Within the Born approximation, the mean free path of the potential we use is estimated to have a value of $4 \times 10^3 a$ which is much longer than the system size so that we are in the ballistic regime. The mobility corresponding to these parameters is of the order $2 \times 10^6 \text{ m}^2/\text{Vs}$.

In Fig. 10a, the calculated current density is seen to exhibit a branching behavior that was also apparent in the experiment in Ref. 7. The branched flow is also present in the map of the conductance difference versus the tip position, when the tip is used as a local scatterer (Fig. 10b). It is clear that there is a direct correspondence between the current density calculation and the conductance map. Therefore one can conclude that the experiment in Refs. 6, 7 really probes the current distribution in the sample. Also visible in the conductance difference map are the interference fringes spaced by half

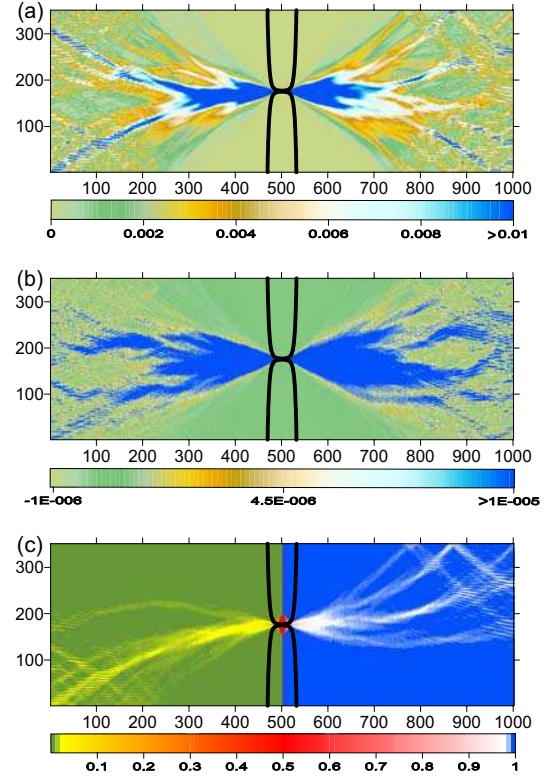


FIG. 11: Maps of electron flow through a quantum point contact with a moderate magnetic field. Lengths on the axes are given in units of the lattice parameter a . Transport current density distribution (a) in units of $2e^2V = (\hbar a)$, STM conductance map (b) (conductance is measured in units of $2e^2 = \hbar$) and STM voltage probe map (c). The voltage on the left lead $V_L = 0$, and voltage is measured in units of V_R . The Fermi energy contour is depicted in black.

the Fermi wavelength, which were explained as resulting from scattering between the point contact and the STM tip⁶. The map of the local chemical potential, as measured by the STM voltage probe (Fig. 10c) in this case gives similar information as the previous plots: on the left the current flow appears as regions (yellow) with increased voltage compared to that of the left lead (green). This corresponds to a decreased chemical potential due to a deficit of electrons resulting from the non-equilibrium transport process. On the right, the current flow appears as regions (white) with a decreased voltage compared to the right lead (blue). This corresponds to an increased chemical potential (excess electrons due to the transport process).

In Fig. 11, the quantities are calculated for the same system as before, but now a magnetic field is included. The field is characterized by a magnetic length of $l_B = 28a$, and a cyclotron radius $r_c = 835a$. From the non-equilibrium transport current density plot (which is symmetric in the magnetic field), it is clear that the branches of electron flow start bending. The radius of curvature has the same order of magnitude as the cyclotron radius,

so we are seeing here the onset of the skipping orbit movement of the electrons. The branches are reflected on the upper and lower edges of the sample, a proof that one is still in the ballistic regime. The conductance difference map (Fig. 11b) is quite unclear (note that the highest value on the conductance scale is 10 times smaller compared to Fig. 10b). This was explained as resulting from the reduction of backscattering in the presence of a magnetic field (section IIB). But nevertheless the tendency of the branches to curve can be observed. In this regime, the voltage probe method gives better results. The curved branches are clearly visible in Fig. 11c. Please keep in mind that the voltage method is not symmetric under reversal of the field, which results in the asymmetry of the voltage map. This asymmetry will be explained in more detail with the help of Fig. 12c.

In Fig. 12, results are shown for a high magnetic field (magnetic length $l_B = 4.8a$, cyclotron radius $r_c = 24a$). In a plot of the transport current density the electrons are seen to describe skipping orbits along the edges of the sample; we are in the quantum Hall regime. It was explained that in this regime the original tip scattering method fails because of a lack of backscattering. This is visible in Fig. 12b: only in the middle of the quantum point contact there is some conductance decrease because in this region waves travelling in opposite directions are "forced" to overlap. The map of the local chemical potential (Fig. 12c) gives better results: the skipping orbits are clearly visible.

The asymmetry of this plot was already pointed out above, and can be understood as follows: the voltage on the right lead is chosen to be higher than that on the left lead, so electrons are flowing from the left to the right. The magnetic field for this plot is pointing out of the plane of the paper, so the scattering states correspond to those shown in Fig. 6a. Electrons emerging from the left lead flow along the upper left edge of the sample, so this edge is in equilibrium with the left lead (no skipping orbits are seen on this edge, only a uniform potential distribution). Some of these electrons are transmitted through the point contact, which results in a higher chemical potential (so lower voltage!) than μ_R at the upper right edge of the sample. The electrons reflected from the contact (continuing their path on the lower edge) give rise to a chemical potential that is lower (= voltage that is higher) than μ_L (V_L) on the lower left edge.

The edge states are also apparent in a plot of the local density of states at the Fermi energy (Fig. 12d). The electrons seem to be reflected on the left and right side, where the sample connects to the leads. This is because they are scattered on the impurity potential step at the lead-sample interface (no impurity potential in the leads). In a plot of the equilibrium current, Fig. 12e, a fraction of the currents are seen to flow along the sample edges, but because of the impurities there are also persistent currents flowing in the middle of the sample. Again, the currents are reflected on the device-lead interface. This reflection was not visible in a plot of the transport cur-

rent because the reflected currents are asymmetric in the magnetic field.

For completeness, we have also shown the electron particle density in Fig. 12f. The energy integration necessary for the calculation of the electron density and equilibrium current density was performed along a half circle in the complex plane, as shown in Fig. 5. The integration points were chosen with the Gauss-Legendre method; they are more densely spaced in the regions close the real axis. For this problem, convergence was reached after 16 integration points (the results did not change in 8 significant digits after doubling the number of points to 32).

VI. CONCLUSION

We have established an efficient tight-binding method to numerically calculate spatial maps of electron flow as obtained in a recent series of scanning probe experiments where an STM tip is used as a local scatterer for electrons⁶. The computational effort of our numerical approach scales like M^3N (in the limit $N \gg 1$), where M is the width of the lattice and N is the length. It is in this way more efficient than the standard recursive Green's function method which scales like M^4N^2 for the same problem.

We have also shown expressions for the local density of states, the electron density and the current density distribution. These quantities cannot be calculated within the standard recursive approach, but within our scheme they can be expressed in terms of the same Green's functions already known from the numerical simulation of the scanning probe experiment. The computational effort for these quantities also scales as M^3N .

When a magnetic field is applied, backscattering of electrons will be strongly reduced because of the presence of edge states so that the original STM method does not give the desired results. Therefore, a new probe method was proposed where the tip is used to measure the local chemical potential. For this problem again, the numerical effort scales like M^3N . The image one obtains from such a method is not always directly related to the current pattern in the sample, but one can expect to obtain relevant information about transport in the sample. Furthermore, a discussion was included on how to define a pure transport current density in a physically meaningful way when a magnetic field is present.

The power of the method was proven in example calculations, where a tight-binding lattice with more than 350000 sites has been used. Moreover, by direct comparison between a numerical simulation of the experiment and a calculation of the exact current density distribution, it became clear that the original scanning probe technique of Topinka et al.⁶ is really imaging current flow.

It should be clear that the method proposed is very general, and the information obtained by the different imaging tools very broad, so that it can be used to study electron flow in a variety of systems ranging from e.g.

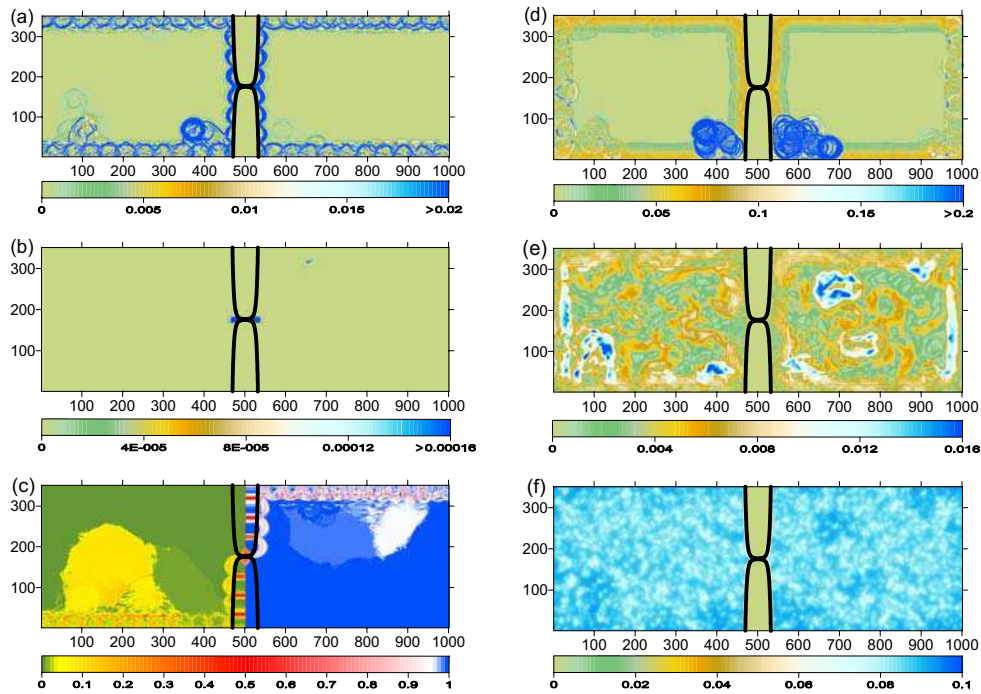


FIG. 12: Maps of electron flow through a quantum point contact with a high magnetic field. Lengths on the axes are given in units of the lattice parameter a . Transport current density distribution (a) in units of $2e^2V = (\hbar/a)$, STM conductance map (b) (conductance is measured in units of $2e^2/\hbar$) and STM voltage probe map (c). The voltage on the left lead $V_L = 0$, and voltage is measured in units of V_R . Plots of the local density of states (d) (units $1 = (a^2 t)$), the equilibrium current (e) (units $2et = (\hbar/a)$) and electron particle density (f) (units $1 = a^2$) are also shown. The Fermi energy contour is depicted in black.

the quantum Hall effect to quantum chaos in electron billiards¹⁶. Moreover, including the spin degrees of freedom proves to be rather easy; every matrix element should be

replaced by a spinor. As such, an even broader range of phenomena could be studied, ultimately also those including spin-orbit coupling (e.g. the spin Hall effect^{17,18}).

Electronic address: georgo@mpi-halle.de

^y Electronic address: bruno@mpi-halle.de

^z URL: <http://www.mpi-halle.de>

¹ S. Datta, *Electronic Transport in Mesoscopic Systems*, (Cambridge University Press, England, 1995).

² D. K. Ferry and S. M. Goodnick, *Transport in Nanostructures*, (Cambridge University Press, England, 1997).

³ B. J. van Wees, H. van Houten, C. W. J. Beenakker, J. G. Williamson, L. P. Kouwenhoven, D. van der Marel, and C. T. Foxon, *Phys. Rev. Lett.* **60**, 848 (1988).

D. A. Wharam, T. J. Thornton, R. Newbury, M. Pepper, H. Ahmed, J. E. Frost, D. G. Hasko, D. C. Peacock, D. A. Ritchie, and G. A. C. Jones, *J. Phys. C* **21**, L209 (1988).

⁴ K. v. Klitzing, G. Dorda, and M. Pepper, *Phys. Rev. Lett.* **45**, 494 (1980).

⁵ P. A. Lee, A. D. Stone, and H. Fukuyama, *Phys. Rev. B*, **35**, 1039 (1987).

⁶ M. A. Topinka, B. J. LeRoy, S. E. J. Shaw, E. J. Heller, R. M. Westervelt, K. D. Maranowski, and A. C. Gossard, *Science* **289**, 2323 (2000).

⁷ M. A. Topinka, B. J. LeRoy, R. M. Westervelt, S. E. J. Shaw, R. Fleischmann, E. J. Heller, K. D. Maran-

owski, and A. C. Gossard, *Nature* **410**, 183 (2001).

⁸ B. J. LeRoy, *J. Phys.: Condens. Matter* **15**, R1835 (2003).

⁹ M. Buttiker, *Phys. Rev. Lett.* **57**, 1761 (1986).

¹⁰ G.-P. He, S.-L. Zhu, and Z. D. Wang, *Phys. Rev. B* **65**, 205321 (2002).

¹¹ A. Cresti, R. Farchioni, G. Grosso, and G. P. Parravicini, *Phys. Rev. B* **68**, 075306 (2003).

¹² D. Guan, U. Ravaioli, R. W. Giannetta, M. Hannan, I. A. Desida, and M. R. Melloch, *Phys. Rev. B* **67**, 205328 (2003).

¹³ M. P. Lopez Sancho, J. M. Lopez Sancho, and J. Rubio, *J. Phys. F* **15**, 851 (1985).

¹⁴ I. Turek, V. Drahfal, J. Kudrnovsky, M. Sob, and P. Weinberger, *Electronic structure of disordered alloys, surfaces and interfaces*, (Kluwer, Boston, 1997).

¹⁵ J. H. Davies, *The physics of low-dimensional semiconductors: an introduction*, (Cambridge University Press, Cambridge, 1998).

¹⁶ C. M. Marcus, A. J. Rimberg, R. M. Westervelt, P. F. Hopkins, and A. C. Gossard, *Phys. Rev. Lett.* **69**, 506 (1992).

¹⁷ J. E. Hirsch, *Phys. Rev. Lett.* **83**, 1834 (1999).

¹⁸ J. Sinova, D. Culcer, Q. Niu, N. A. Sinitsyn, T. Jungwirth, and A. H. MacDonald, *Phys. Rev. Lett.* **92**, 126603 (2004).

